nature materials

SUPPLEMENTARY INFORMATION

DOI: 10.1038/NMAT5034

In the format provided by the authors and unedited.

Dislocation nucleation facilitated by atomic segregation

Lianfeng Zou[1], Chaoming Yang[2], Yinkai Lei[3], Dmitri Zakharov[4], Jörg M.K. Wiezorek[3], Dong Su[4], Qiyue Yin[1], Jonathan Li[5], Zhenyu Liu[3], Eric A. Stach[4], Judith C Yang[6], Liang Qi[2], Guofeng Wang[3], Guangwen Zhou[1*]

[1]Department of Mechanical Engineering & Materials Science and Engineering Program, State University of New York at Binghamton, NY 13902

[2]Department of Materials Science and Engineering, University of Michigan, Ann Arbor, MI 48109

[3]Department of Mechanical Engineering and Materials Science, University of Pittsburgh, Pittsburgh, PA 15261

[4]Center for Functional Nanomaterials, Brookhaven National Laboratory, Upton, NY 11973

[5]Department of Physics, Applied Physics and Astronomy & Materials Science and Engineering Program, State University of New York, Binghamton, NY 13902

[6]Department of Chemical and Petroleum Engineering, University of Pittsburgh, Pittsburgh, PA 15261

[*] Correspondence to: gzhou@binghamton.edu

This file includes:

Extended sections 1 to 14

Extended Data Tables 1-2

Extended Data Figures 1 to 14

Captions for Supplemental Videos 1 to 7

References

Other Supplementary Materials for this manuscript includes the following:

Supplemental Videos 1 to 7

Extended Data Section 1. Edge thinning under the strong electron beam condition (Extended Data Figures 1 and 2)

Edge thinning effects can be observed in the environmental TEM (ETEM) experiments with a strong electron beam current and in STEM experiments with a condensed beam probe. Extended data Figs. 1(a-b) show a typical example of the edge thinning along the (110) facet while we deliberately used a strong beam to focus on the edge area, which resulted in the edge thinning along the (110) edge, as shown by the significantly weakened image intensity of the characteristic Au-segregation induced trough-crest surface reconstruction. Meanwhile, the electron-beam induced edge thinning led to the formation of a new (110) ledge that is three atomic layers away from the old one. The Au segregation along the newly formed (110) ledge resulted in the same characteristic trough-crest surface reconstruction, as shown in the HRTEM image (Extended data Fig.1b). This indicates that the intense beam illumination can facilitate the knock off of atoms from the edge area and lead to the edge thinning. However, the edge thinning effect is negligible when we spread the e-beam, which was the typical operation condition that we used for capturing the (110) surface dynamics in the TEM model shown in the manuscript.

In the STEM model, the beam effect could be more significant because of the higher probe current density and longer acquisition time required for STEM imaging. The e-beam induced edge thinning effect can be also seen from the STEM image (Extended data Fig.1c), where the scanning process along the (110) facet knocked out some surface atomic columns, and the remaining surface columns are still visible, as pointed by the white arrows.

We also acquired HAADF images with various detector collection angles by changing the camera length to check for any variation in image contrast. For example, we collected images using the inner angles of 54 mrad, 68 mrad and 90 mrad, which correspond to the camera length of 10 cm, 8 cm and 6 cm, respectively. All of the STEM images consistently showed the edge thinning effect (please see Extended Fig. 2), which allowed us to rule out any potential effect from the collection angle induced surface contrast changes. We also compared the STEM images acquired at 350 °C and room temperature, both of which showed the characteristic trough-crest Cu_3Au surface contrast without visible contrast difference

on the topmost layer, indicating the negligible temperature effect (i.e., the Debye-Waller effect) on the image contrast.

Extended Data Section 2. HRTEM image simulations (Extended Data Figure 3)

The formation of faceted holes in the Cu-Au thin films during the oxide removal annealing may result in some edge thinning relative to the original bulk thin film thickness. We performed HRTEM image simulations to ascertain the origin of the atomic column contrast difference between the surface region and the bulk. The simulated HRTEM images obtained using the Cu_3Au segregated configuration consistently reproduced the characteristically darker Au atom column contrast for the surface region relative to the Cu(Au) alloy lattice of the bulk region (Fig. 1e). On the contrary, the simulated HRTEM images obtained using model crystals with a reduced thickness at the outermost surface (Extended data Fig. 3), considering the effect of edge thinning, produced more uniform contrast of the atom columns in both the surface and bulk alloy regions, which is inconsistent with the experimental observations. The HRTEM image contrast simulations further confirm that the experimentally observed {100}-type nano-facets of the trough-crest reconstructed (110) surface are attributed to the Cu_3Au segregated configuration.

Extended Data Section 3. DFT simulation (Extended Data Figure 4)

The reconstructed (110) surface of the $Cu_{90}Au_{10}$ alloy was modeled by a slab with one bulk terminated (110) surface and one (2×1) reconstructed (110) surface as shown in Extended data Fig. 4. 15 atomic layers were used in all models with 58 atoms in total. The trough-crest reconstructed (110) surface in the TEM image shows ordering similar to the (110) surface of Cu_3Au. Therefore, three possible terminations of the reconstructed (110) surface of Cu_3Au were used on the reconstructed surface of the slab (Extended data Figs. 4(b-d)). Moreover, a model with randomly distributed Au atoms was built as a reference (Extended data Fig. 4e). In all these models, the number of Au atoms in bulk was adjusted in order to keep an overall Au concentration of 10.3 at. % (6 Au atoms). Besides, the bottom 5 layers of the super cells were fixed in all the models (see Extended data Fig. 4a). The lattice constant (3.759 Å) was

determined by a linear interpolation between the lattice constant of pure Cu (3.622 Å) and Au (4.175 Å). All models were relaxed until the Hellman-Feynman force exerted on each atom was less than 0.01 eV/Å.

The stability of each possible termination was measured by the energy difference between the corresponding model and the random model. We found that the energies of the models in Extended data Figs. 4b and 4d are lower than the energy of the random model by 302.2 mJ/m^2 and 145.6 mJ/m^2, respectively. On the contrary, the energy of the structure shown in Extended data Fig. 4c is 239.8 mJ/m^2 higher than the energy of the random model (Extended data Fig. 4e). Therefore, the Cu_3Au type termination of ordering as shown in extended data Fig. 4b is predicted to be the most energetically favorable termination among the four modeled terminations on the reconstructed (110) surface of $Cu_{90}Au_{10}$.

Extended Data Section 4. Calculation of the critical thickness of the coherent Cu_3Au segregated layer

According to the classical Matthews-Blakeslee model for the onset of misfit dislocations in thin films on the bulk substrate, the interfacial misfit dislocations can be generated if the thickness of the thin films is above a critical value h_c. Corrected for a single array of misfit dislocations in two dimensions, h_c can be obtained by numerically solving the following equation[1]

$$h_c = \frac{b}{8\pi(1+v)f}\left[\ln\left(\frac{h_c}{b}\right)+1\right].$$

Here v is Poisson ratio and v = 1/3; b is the length of Burgers vector and it equals to $\frac{\sqrt{2}}{2} \times a_{Cu_3Au}$= 2.65 Å ($a_{Cu_3Au}$=3.75 Å); f is the misfit strain that can vary on the scale of 2~3% depending on the local Au concentrations. By numerically solving the above equation, we can find that the critical thickness varies from 3.43 Å to 8.62 Å with the strain changing from 2.9% to 2.0%.

Extended Data Section 5. In-situ TEM visualization of the decay of pairs of atomic columns of Au from the (110) surface (Extended Data Figure 5)

Extended Data Section 6. Locate the misfit dislocation nucleation site (Extended Data Figure 5 and Figure 6)

Surface atoms tend to peel off as pairs of atomic columns and the troughs thus maintain the same depth, i.e., three atomic layers deep from the outermost row of the (110) surface, thereby maintaining the coherent Cu_3Au/Cu(Au) interface structure (Extended data Fig. 5). However, occasionally a deeper trough develops locally when two pairs of atomic columns migrate away from the same trough region, which results in the birth of a unit dislocation at the highly strained location along the Cu_3Au/Cu(Au) interface. The removal of four atomic columns can be confirmed from the still images (Extended data Figs. 6(c-d) extracted from the in-situ TEM video frame by frame. Extended data Figs. 6(c-d) are the raw images of Figs. 2(a-b) and the two circled regions correspond to the same region, which can be used as the marker to track the changes in the distance between the outermost surface and the circled regions between the two consecutive TEM images. As can be seen in Extended data Fig. 6c, the outermost surface and the marker lattice point has a distance of 16 $d_{(020)}$ lattice spacings along the vertical direction, which then decreases to 14 $d_{(020)}$ lattice spacings in Extended data Fig. 6d, indicating the removal of two atomic columns along the [200] direction. Similarly, the distance between the outermost surface and the marked lattice point along the horizontal direction decreases from 20 $d_{(200)}$ lattice spacings to 18 $d_{(200)}$ lattice spacings between the two consecutive TEM images, due to the peeling off of two columns of atoms along the [020] direction. Therefore, there are a total of four columns of surface atoms that have peeled off from the circled region shown in Figs. 2(a-b) during the time interval of 0.5 s, which results in a locally deepened trough (four atomic layers deep).

Extended Data Section 7. DFT modeling of the stability of surface atoms (Extended Data Figure 7)

The physical reason for the departure of four columns of surface atoms can be related to the locally insufficient Au segregation, for which the surface tends to develop locally a deeper trench for initiating dislocation nucleation (i.e., Fig. 2). To address this question, we employed DFT to calculate the stability

of the surface atoms. Extended Data Figure 7 shows the surface configuration of the $L1_2$ ordered Cu_3Au segregated layer based on our experiment result (e.g., Figs. 1 and 2). We then calculated the vacancy formation energy by removing each of the atoms (labeled 1, 2, 3 and 4) in the four columns of surface atoms. The DFT results (see Extended Data Table 1) show that the energy cost for removal of the outermost atom (atom 1) is 0.28 eV. After atom 1 has been removed, the energy barrier for the removal of atom 2 is only 0.07 eV. This is a strong indication that atom 2 becomes highly unstable once losing the protection from the outermost Au atom (i.e., atom 1) and is thus prone to diffuse away together with atom 1 instead of detaching individually. This is consistent with our in-situ TEM observation that shows that surface atoms detach from the surface in pairs of Cu and Au atoms (please see Supplementary in-situ TEM video 1).

The departure of surface pairs (atoms 1 and 2) leads to the exposure of very unstable surface sites (atom 3). The energy cost for vacancy formation at site 3 is -0.33 eV, which indicates that the removal of atom 3 is a spontaneous process. The further removal of atom 4 is slightly less that the removal of the Au atom at site 1. However, if Au surface segregation is sufficiently fast to replace the Cu atom at site 3 during the decay of the surface pair of atoms 1 and 2, this can improve the stability of the Cu and Au pair at sites 3 and 4. Therefore, the reason for the departure of more surface atoms from a localized region can be attributed to the stochastic process of locally insufficient Au segregation, for which the exposed Cu atoms are more vulnerable to decay from the surface, thereby developing into a locally deeper trench.

Extended Data Table 1: DFT computed vacancy formation energies for removing atoms 1-4 labeled in Extended data Fig.7

Site	Vacancy Formation Energy (eV)
1	0.28
2	0.07
3	-0.33
4	0.25

Extended Data Section 8. Locate dislocation positions from IFFT and identify the core structure of the dislocations in the parent Cu(Au) region (Extended Data Figure 8)

HRTEM image simulations are used to identify the core structure of the dislocations in the parent Cu(Au) region using different configurations of the dislocation lines. Extended data Figs. 8(d-h) show the simulated HRTEM images obtained from several representative structure models including three configurations with different inclined dislocation lines and one example with a screw component for the unit dislocations with line direction [001]. Their comparison shows that the one with the pure edge component ($\mathbf{b} = \frac{1}{2}a[\bar{1}10](110)$ provides the best match with the experimental HRTEM images, where the dislocation core only affect the contrast of a very localized area, whereas the other core structures affect the image contrast of a larger area.

Extended Data Section 9. Random walk characteristic of dislocation cores (see Extended Data Figure 9)

The migration trajectories can be tracked after the dislocations move into the parent Cu(Au) area. Extended data Figs. 9(a-d) depict a sequence of in-situ TEM images showing the migration path of a misfit dislocation in the parent Cu(Au) region. Extended data Fig. 9(e) shows the distance of the dislocation from its initial location as a function of time. At first, the dislocation is observed to oscillate at a stand-off distance of about 4 ~ 6 d_{220} lattice spacings (i.e., a distance of 1 nm to 1.5 nm from the Cu_3Au/Cu(Au) interface). It is surprising to note from the in-situ TEM observations (Supplementary in-situ TEM videos 6 and 7) that the motion by glide and climb is of similar probability once the dislocation fluctuates at a stable distance, which is the typical feature of a random walk. To confirm the nature of the random walk of the dislocation motion, the mean displacements of the dislocation core are obtained from frame-by-frame measurements on individual images of the in-situ TEM video. In our analysis, 40 time-sequential TEM images were used. For each time interval (i.e., Δt = 1 s, 2 s, 3 s, etc.), there are 20 displacements used for averaging. For example, the 20 displacements for Δt = 1 s are those between t_1= 0

s and t_2 = 1 s, t_2 = 1 s and t_3 = 2 s, t_3 = 2 s and t_4 = 3 s, etc.; the 20 displacements for Δt = 2 s are those between t_1= 0 s and t_3 = 2 s; t_2 = 1 s and t_4 = 3 s, t_3 = 2 s and t_5 = 4 s, etc., where t_1, t_2, t_3, …, correspond to the time-sequence TEM images. The starting location of the dislocation is given in the first TEM image (i.e., t_1 = 0 s). The mean square displacements (MSD) $\bar{d}^2$ for each time interval Δt is calculated using the following equation,

$$\bar{d}^2(\Delta t) = \frac{1}{40 - \Delta t + 1} \sum_{t=0}^{40-\Delta t} [\vec{r}(t + \Delta t) - \vec{r}(t)]^2 ,$$

where $\vec{r}(t)$ is the displacement vector of the dislocation at time t with respect to the moment (t – Δt). Therefore, the calculated results $\bar{d}^2$ represent the average over different sets of motions. As shown in extended data Fig. 9(f), the MSD of the dislocation core increases linearly with time, indicative of a standard random walk characteristic. The error bars in Extended data Fig. 9(f) are the uncertainties $e(\Delta t)$ calculated based on the variation of the square displacements at each time interval, which can be defined as the square root of the quotient of the variation by the number of data points, as described by the following equation,

$$e(\Delta t) = \sqrt{\frac{\overline{d^4}(\Delta t) - \left[\overline{d^2}(\Delta t)\right]^2}{n(\Delta t) - 1}} ,$$

where $\overline{d^4}(\Delta t)$ is the average of fourth power of the displacement, $\overline{d^2}(\Delta t)$ is the mean square displacement and $n(\Delta t)$ is the number of data points at Δt. Note that there are no error bars in Extended data Fig. 9(e) because there is only one displacement for each point. The diffusivity of the dislocation core is estimated to be 0.27 Å^2/s with an uncertainty of ±0.03 Å^2/s.

Extended Data Section 10. DFT calculation of GSF curve and APB energy (Extended Data Figure 10)

We apply density functional theory (DFT) calculations to obtain the generalized stacking fault (GSF) energy along the $[\bar{1}10](110)$ slip system as well as the ½$[\bar{1}10](110)$ antiphase boundary energy of

$L1_2$ Cu_3Au. The DFT calculation is performed on VASP[2] with non-spin-polarized conditions. The pseudopotentials of Cu and Au are obtained by the projector augmented wave method (PAW)[3] with the Perdew-Burke-Ernzerhof exchange-correlation functional (PBE)[4]. We take the first-order Methfessel-Paxton smearing of 0.4 eV for partial occupancies of each orbital and kinetic cutoff energy of 360.00 eV throughout the calculation.

In the calculation of the GSF along $[\bar{1}10](110)$, our calculation cells take X, Y, Z base vectors along the direction of $[\bar{1}10]$, [001] and [110], respectively. For pure Cu, we take the (2.6 Å × 3.7 Å × 31.4 Å) supercell of 20 atoms and mesh the K-points by (18 × 18 × 1) with the Monkhorst-Pack scheme. We also construct the (5.2 Å × 7.4 Å × 31.4 Å) supercell of 79 Cu atoms and 1 Au atom to calculate the GSF along $[\bar{1}10](110)$ under the Au alloying effect, where the Au atom is located on the (110) layer nearest to the glide interface (Extended data Fig. 10(a)). The K-points are the (11 × 11 × 1) Monkhorst-Pack mesh. We implement the selective dynamics scheme such that all atoms are allowed to move only along the [110] direction during relaxation, which is perpendicular to the (110) glide interface. We sample ten equidistance configurations as shifting the (110) plane of the supercell along $[\bar{1}10]$ to calculate the energy and perform cubic spline interpolation in order to obtain the GSF curve of the (110) plane glide along the $[\bar{1}10]$. Our calculation shows that the Au solute on (110) layer nearest to the glide interface increases the unstable stacking fault along $[\bar{1}10](110)$ by ~50 meV/m^2. In addition, we extend our calculations of GSF for all possible vectors on the (110) slip plane, which shows no local minimum of GSF energies except those corresponding to the full Burgers vector of $\frac{1}{2}[\bar{1}10]$ in either pure Cu and Cu(Au) alloys, which suggests no stable configurations of partial dislocation Burgers vectors on this slip plane.

In calculation of the APB along (110) of the $L1_2$ Cu_3Au structure, we build the ordered $L1_2$ Cu_3Au supercell of 36 Cu atoms and 12 Au atoms, with the supercell size of (5.7 Å × 4.1 Å × 40.2 Å) (extended data Fig. 10(b)). The basic Cartesian vectors are chosen along $[\bar{1}10]$, [001], [110], respectively, and K-points are meshed by (21 × 21 × 1) to ensure convergence. We add $\frac{1}{2}[\bar{1}10]$ shift on half of the (110)

planes of the supercell to generate the APB configuration and calculate the energy of the supercell with and without APB. The DFT results show that the APB energy along the (110) plane of $L1_2$ Cu_3Au is 0.1097 eV/A^2.

Extended Data Section 11. Blocking effect of the $L1_2$ Cu_3Au segregated layer on dislocation penetration (see Extended Data Figure 11)

The initial configuration of the ½ $[\bar{1}10]$ edge dislocation is generated by displacing atoms according to the continuum displacement field of edge dislocations [5] with static minimization of the system energy. According to the size of the experimental samples, we take the 56 nm × 44 nm × 3 nm simulation box of 463000 atoms, with the fixed boundary condition along x and y directions and periodic boundary condition along the z-direction. All of the potentials employed in calculations of the near-surface ½ $[1\bar{1}0]$ edge dislocation provide well-consistent result that the dislocations without the APB barrier annihilate on the free surface in pure Cu within several picoseconds by local diffusionless transformation (Extended data Figs. 11(b, d)).

In addition, via calculations of two different configurations of surface atomistic structures (i.e., the perfect (1×1) surface and the experimentally observed (2×1) reconstruction), we verify that the dislocation is dragged to the free surface and annihilate regardless the different surface configurations for pure Cu. We estimate the energy decrement by calculating the energy difference before and after the dislocation annihilation on the free surface, and find the energy decreases by 0.685 eV/Å in the case of the (2×1) reconstructed surface and 0.343 eV/Å for the non-reconstructed surface.

To be consistent with the experimental observations that the near-surface dislocations can exist for several seconds and even much longer time, we construct three surface layers of $L1_2$ Cu_3Au with the (2×1) reconstruction on the bulk substrate with randomly 10 atomic percent of Au in the Cu lattice. We also introduce the ½$[\bar{1}10](110)$ edge dislocation in the bulk slightly below the ordered $L1_2$ Cu_3Au surface layer. By tuning the initial position of the dislocation and running MD simulation for ~10 nanoseconds at

600 K, we verify that the dislocation glides along the Cu_3Au/Cu(Au) interface without entering the Cu_3Au segregated layer (Extended Data Fig. 11(a)). By ignoring the chemical effect of Au atoms, we perform the same calculation on the Cu-Ag system based on the Cu-Ag EAM potential[6]. We introduce three layers of the $L1_2$-Cu_3Ag as the segregated surface layer on the bulk substrate with randomly 10 atomic percent of Ag atoms in Cu lattice. The MD simulation still shows the dislocation glide along the $L1_2$-Cu_3Ag/Cu(Ag) interface without penetrating through the Cu_3Ag layer (Extended data Fig. 11(c)), indicating that the stability of near-surface dislocations is significantly enhanced by the presence of the chemically ordered structure of the segregated layer.

In the simulation of the formation of APB, we modify the initial position of the ½[$\bar{1}$10](110) edge dislocation to generate the dislocation within the $L1_2$-ordered Cu_3Au segregated layer, then run MD for 100 picoseconds (Figs. 4(c-d)). After the energy minimization, we find that the system energy increases by ~21 eV with the presence of an APB, which illustrates that the large energy barrier for the APB formation prevents the dislocation from entering the Cu_3Au segregated layer. In fact, the energy increase due to APB is proportional to the total APB area. Because the energy decrease due to surface dislocation annihilation is on the scale of 0.5~1 eV/Å from the above MD simulations, and the APB energy cost is on the scale of 0.1 eV/ A^2 from first-principles calculations in Extended data section 11, it means that the APB can prevent the dislocation annihilation as long as its length along the direction perpendicular to the dislocation line ([$\bar{1}$10] in our cases) is about 5~10 Å, which is easy to be achieved in the thin film samples in our experiments.

In verification of the mobility of the ½ [$\bar{1}$10] edge dislocation on the (110) slip plane, we use MD simulations to examine the critical resolved shear stress (CRSS) to drive the ½ [$\bar{1}$10](110) dislocation glide in pure Cu at 630 K. We take the (36 × 25 × 22 nm) simulation box of 1152000 atoms to decrease the pinning effect generated by the periodicity along the z direction. By adding shear strain on the (110) plane at the strain rate of 4.75×10^6 per second, we find the CRSS of the ½ [$\bar{1}$10](110) dislocation of Cu at 630 K is ~11 Mpa, which is generated by 1.55×10^{-4} of shear strain.

Our MD simulation results show that both the perfect and the crest-trough reconstructed Cu3Au (110) surface can effectively block the dislocation motion towards the free surface (Extended Data Figure 11) because the dislocation penetration requires the formation of an APB and thus significantly increases the system energy. On the other hand, dislocations easily migrate to the surface for both the perfect and reconstructed (110) surfaces for pure Cu (Extended Data Figure 11). These results further confirm that that it is the development of the Cu3Au surface alloy to stabilize the sub-surface dislocations and their subsequent migration is dominated by the interplay between the composition fluctuations and the image force.

Extended Data Section 12. Investigations on the near-surface dislocation behavior using the continuum elastic theory and its comparison with MD simulations (Extended Data Figures 11(e, f) and Extended Data Table 2)

A: Stress distribution due to surface image effect

To calculate the stress on the near-surface dislocation, we first construct the image dislocation whose stress distribution cancels parts of the initial edge dislocation (Extended data Fig. 11(e)). With the image, the only stress left along the surface equals

$$\sigma_{xy}(x, y=l) = 2\frac{\mu b}{2\pi(1-\nu)}\frac{x(x^2-l^2)}{(x^2+l^2)^2} \quad (1)$$

Thus, to obtain the free-of-stress surface, the stress function ϕ needs to be established to cancel the stress given by Eq. 1. To solve the biharmonic equation,

$$\frac{\partial^4\phi}{\partial x^4} + 2\frac{\partial^4\phi}{\partial x^2\partial y^2} + \frac{\partial^4\phi}{\partial y^4} = \nabla^4\phi = 0 \quad (2)$$

,

We use the separation of the variable method, and assume that the Airy stress function takes the form $\phi = X(x)Y(y)$ such that

$$\frac{\partial^4 Y}{\partial y^4} + \frac{2}{X}\frac{\partial^2 X}{\partial x^2}\frac{\partial^4 Y}{\partial y^2} + \frac{Y}{X}\frac{\partial^4 X}{\partial x^4} = 0 \quad (3)$$

,

which has the solution $X = \alpha\cos(kx)+\beta\sin(kx)$, where k is a free parameter. Therefore, the biharmonic equation becomes

$$\frac{\partial^4 Y}{\partial y^4} - 2k^2\frac{\partial^2 Y}{\partial y^2} + k^4 Y = 0 \quad (4)$$

which has the solution $Y = (a+by)e^{ky} + (c+dy)e^{-ky}$. We then consider the boundary conditions as $y \to \infty$, $Y = 0$, therefore, $a = b = 0$, and $Y(y=0,x) = 0$ gives $c = 0$, thus $Y = dye^{-ky}$. We also notice that the derivative of the Airy stress respective to x produces an odd function, thus, we drop the $\sin(kx)$ term in $X(x)$. Furthermore, since the parameter k can be any value to satisfy the equation, based on the sum rule, the solution is given by

$$\phi = \int_0^\infty \alpha(k) y e^{-ky}\cos(kx)dk \quad (5)$$

The boundary condition on the free surface generates

$$\left(\frac{\partial^2\phi}{\partial x\,\partial y}\right)_{y=0} = -\sigma_{xy}(x, y=0) = -\int_0^\infty \alpha(k)k\sin(kx)dk = \frac{\mu b}{\pi(1-\nu)}\frac{x(x^2-l^2)}{(x^2+l^2)^2} \quad (6)$$

It is the form of Fourier Integral formula, thus

$$\alpha(k)k = -\frac{\mu b}{\pi^2(1-\nu)}\int_{-\infty}^{\infty}\frac{x(x^2-l^2)}{(x^2+l^2)^2}\sin(kx)dx \quad (7)$$

We decrease the order of x via integration by parts, then utilize the residue theorem to integrate. After one step of integration by parts, Eq. 7 becomes

$$\alpha(k)k = \frac{\mu b}{\pi^2(1-\nu)}\frac{1}{k}\int_{-\infty}^{\infty}\frac{x^4-6x^2l^2+l^4}{(x^2+l^2)^3}\cos(kx)dx \quad (8)$$

By using the residue theorem, we finally obtain

$$\alpha(k) = \frac{\mu b}{\pi(1-\nu)}(l - \frac{1}{k})e^{-kl} \quad , \tag{9}$$

$$\phi = \frac{\mu b}{\pi(1-\nu)}\left[\frac{ly(l+y)}{(l+y)^2+x^2} - \int_0^\infty \frac{1}{k} e^{-k(y+l)} y\cos(kx)\,dk\right] \quad . \tag{10}$$

We calculate the force that attracts the dislocation toward the free surface as the following: based on the Peach-Koehler equation, $\vec{F} = (\sigma\vec{b})\times\vec{\xi}$, where the σ, $\vec{b}$ and $\vec{\xi}$ are the stress matrix, the Burgers vector and the unit dislocation line vector, respectively. The force acting on the dislocation is $\vec{F} = [F_x, F_y, F_z] = [\sigma_{xy}b, \sigma_{xx}b, 0]$, where σ_{xy} and σ_{xx} are stress components and b is norm of the Burgers vector. The force component that drives the dislocation to climb depends on σ_{xx}. Since the Airy stress satisfies

$$\sigma_{xx} = \frac{\partial^2 \phi}{\partial y^2} \quad , \tag{11}$$

and substituting ϕ by (10), we have

$$\sigma_{xx} = \frac{\mu b}{\pi(1-\nu)}\{\frac{2l(x^4 - 3x^2y(l+y) - l(l+y)^3)}{[x^2+(l+y)^2]^3} + \frac{2(l+y)^3 + 2(l+y)x^2 - y(l+y)^2 + yx^2}{[(l+y)^2+x^2]^2}\} \quad , \tag{12}$$

such that

$$\sigma_{xx}(x=0, y=l) = \frac{\mu b}{\pi(1-\nu)}\frac{1}{2l} \quad . \tag{13}$$

The stress generated by the image dislocation is

$$\sigma_{xx}^i = -\frac{\mu b}{2\pi(1-\nu)}\frac{1}{2l} \quad . \tag{14}$$

Therefore, the stress exerted on the dislocation by the free surface is

$$\sigma_{xx}^s = \sigma_{xx} + \sigma_{xx}^i = \frac{\mu b}{4\pi(1-\nu)}\frac{1}{l} \quad , \tag{15}$$

which drags the dislocation to the free surface.

B: Equilibrium due to the coherent strain and the image force

The coherent strain due to the lattice mismatch at the interface will generate the coherent stress, which also drives the dislocation climb. The strain along the y direction (direction perpendicular to (110) surface) is ignored since there is no lattice misfit involved along the y direction. Following the same plain strain condition assumption and isotropic elasticity, we obtain the coherent stress

$$\sigma_{xx}^{c} = \frac{2\mu\nu}{1-2\nu}(\varepsilon_{xx}+\varepsilon_{zz})+2\mu\varepsilon_{xx} \tag{16}$$

Hence, the total stress σ_{xx}^{t} is the sum of the stress from the free surface and the stress due to the lattice misfit as the following,

$$\begin{aligned}\sigma_{xx}^{t} &= \sigma_{xx}^{s}+\sigma_{xx}^{c} \\ &= \frac{\mu b}{\pi(1-\nu)}\frac{1}{4l}+\frac{2\mu\nu}{1-2\nu}(\varepsilon_{xx}+\varepsilon_{zz})+2\mu\varepsilon_{xx}\end{aligned} \tag{17}$$

We can use the elastic constants of pure Cu (*17*) as the approximation to the $Cu_{90}Au_{10}$ solid solution, i.e., μ ~ 70-76 GPa, and ν~ 0.41-0.42. For the $1/2[110](\bar{1}10)$ edge dislocation, b = $\sqrt{2}/2a$. Thus, by solving the stress equilibrium equation $\sigma_{xx}^{t}=0$, the equilibrium distance of the dislocation to the surface is described as the following,

$$l_c = \frac{1}{4\pi(1-\nu)\left(\frac{2}{1-2\nu}(\varepsilon_{xx}+\varepsilon_{zz})+2\varepsilon_{xx}\right)}b \tag{18}$$

The equilibrium distance sits in the range of ~ 2 Å to 20 Å as the lattice strain varies from 2.0% to 0.2%. The equilibrium distance is well consistent with our experimental observations in Fig. 3.

C: Image dragging force and the energy for surface dislocation annihilation

Based on the Peach-Koehler equation, the dragging force due to surface image effect acting on the dislocation can be written as

$$F_y = \varepsilon_{xx} b = \frac{\mu b^2}{4\pi(1-\nu)} \frac{1}{l} \tag{19}$$

Therefore, the work done by dragging the dislocation is

$$\begin{aligned} W &= \int_{l_1}^{l_2} F_y(x)\, dl = \int_{l_1}^{l_2} \frac{\mu b^2}{4\pi(1-\nu)} \frac{1}{l} dl \\ &= \frac{\mu b^2}{4\pi(1-\nu)} [\log(l_1) - \log(l_2)] \end{aligned} \tag{20}$$

The work in Eq. 20 is the elastic energy variation for the near-surface dislocation climbing from a location at l_1 below the surface to another location at l_2 below the surface. If l_2 is very close to the surface (comparable to the dislocation core radius), the work in Eq. 20 can be regarded as the energy variation for the near-surface dislocation annihilation if the core contribution to the energy variation is ignored. Thus, to verify the accuracy of our model, we compare the energy variation calculated in Eq. 20 and the energy variation from MD simulations of the near-surface dislocation annihilation shown in Fig. 4A (also illustrated in Extended Data Figure 11 (b) and (d)).

Based on our MD simulations of pure Cu in Fig. 4A (also in Extended Data Figures 11(b, d)), the initial distance from the dislocation core to surface l_1 is 3 atomic layers (~ 7.6 Å). We define a cutoff distance dc as the final and closest distance that the dislocation can reach to the surface before its annihilation. According to Eq. 20, we can calculate the work by the dragging force on the dislocation located at l_1 below the surface to $l_2 = d_c$, where d_c is comparable with the radius of the dislocation core (Extended Data Table 2). Our MD simulations show that the energy drop due to the dislocation annihilation on the free surface is 0.685 eV/Å and 0.343 eV/Å, respectively, in the two different (110) surface configurations, i.e., the perfect (1×1) surface and the (2×1) reconstructed surface, as mentioned in Section S11 (also shown in Extended Data Figures 11(b, d)). According to Extended Data Figure 11 and our MD simulations, the minimum l_2 that a dislocation can reach to the top surface before annihilation is

about 1~2 Å for the perfect surface and ~3 Å the (2×1) reconstructed surface, so the elastic energy variation calculated by Eq. 20 with l_1 = 7.6 Å to l_2 = 1.5 Å corresponds to the energy drop from MD simulations for the perfect surface, and the elastic energy variation calculated with l_1 = 7.6 Å to l_2 = 3.0 Å corresponds to the energy drop from MD simulations for the reconstructed surface. As shown in Extended Data Table 2 and Extended Data Figure 11(f), the results based on the continuum elastic theory and our MD simulations agree with each other very well for both perfect surface and reconstructed surface cases.

Extended data Table 2: The work by dragging the dislocation from l_1 below the free surface to l_2 = d_c below the surface based on Eq. 20

Cutoff d_c [Å]	1.0	2.0	3.0
Energy [eV/Å]	0.8506	0.5606	0.3909

Extended Data Section 13. Negligible beam effect on surface restructuring and dislocation motion (Extended Data Figures 12 and 13)

To further check any potential e-beam effects on possible surface restructuring (i.e., to rule them out as possible factors affecting the in-situ TEM results and to ensure that we have studied the intrinsic behavior of the surface phenomena), we employed a first-of-its kind direct electron camera (K2) which allows for fast image acquisition (400 frames per second) with a significantly reduced electron dose rate. We examined the possible effect of electron beam irradiation by comparing the Cu3Au segregated surface structure in areas with and without electron beam irradiation and observed the same Cu3Au segregated structure for both cases. The following figure exemplifies these “comparison” experiments, in which the focusing and crystal zone-axis orientation were performed on an adjacent region of the specimen; the specimen was then moved to the area of interest for quick HRTEM imaging. The experiment was performed starting from a continuous $Cu_{10}Au_{90}$ thin film without any pre-existing holes (Extended data

Fig. 12(a)). The thin film was then annealed at 350 °C and 0.001 Torr of H_2 gas flow to produce holes in the film while the beam was blanked off during the annealing process. After ~ 20 min of annealing, a hole formed in the film when the e-beam was un-blanked for TEM imaging. Extended Data Figure 12(c) illustrates a HRTEM image from the hole edge area, which shows that the characteristic Au-segregation induced trough-crest surface reconstruction of the Cu_3Au surface layer already developed along the (110) facet of the hole edge (where the focusing and crystal zone-axis orientation were performed on an adjacent region of the specimen). These comparison experiments confirm the negligible effect of the electron beam irradiation on the Au-segregation induced formation of the trough-crest reconstructed surface Cu_3Au layer. Conducting experiments of this type to understand the effect of electron irradiation is part of our experimental protocol, and in this case ensured that electron irradiation has a negligible effect on the observed surface evolution.

To rule out any electron beam effect from the in-situ TEM observation on dislocation motion, we first identified a dislocation that has already migrated into the bulk (Extended Data Figure 13(a)). The e-beam was blanked off for a few seconds and then un-blanked for TEM imaging, which showed that the dislocation has undergone some migration by moving toward the surface side by a few atomic spacings without the e-beam irradiation (Extended Data Figure 13(b)). Such TEM observation confirms that the electron beam effect has a negligible effect on the dislocation motion and the dislocation migration that we see are inherent.

Extended Data Section 14. Formation of misfit dislocations by Au surface segregation at 600 °C (Extended Data Figure 14)

Au surface segregation induced dislocation formation was also observed by annealing the $Cu_{90}Au_{10}$ sample at 600 °C and 1×10^{-3} Torr of H_2 gas flow show. Extended data Figs. 14(a, b) are the HRTEM images of the surfaces after Au segregation. Rather than forming the Cu_3Au segregated surface layer at 350 °C, one can note that annealing the sample at 600 °C results in the surface segregation of Au

atoms that further aggregate as Au clusters on both the (100) and (110) surfaces. This is because the Cu_3Au ordered phase is stable only up to 390 °C and the higher annealing temperature significantly promotes the atom mobility for the surface segregation and clustering of Au atoms. Clearly, the HRTEM images show the formation of misfit dislocations at the Au/Cu(Au) interface. The observed dislocation arrays along both the [100] and [110] directions indicates there is a dislocation network at the Au/Cu(Au) interface.

It should be noted that the small magnitude of in-plane misfit strain between the lattices of the Cu(Au) alloy substrate and the segregation layer of Cu_3Au, ~2.7%, can be accommodated elastically and a coherent interfacial structure can be retained under the conditions of the in-situ E-TEM experiments. This permits for mobility of the newly formed interfacial dislocations during the experimental observations. For larger magnitudes of interfacial misfit between the substrate alloy and the segregation facilitated surface layer phase a reduced mobility and transition to a semi-coherent interface structure with formation of a misfit dislocation array can be expected (e.g., at T = 600 °C, Au forms in the segregation layer with ~10-11% lattice misfit and a misfit dislocation array formation would be energetically favorable, and the misfit dislocations should be quite immobile, since they can only accommodate misfit strain while resident in the interface as well as the strong dislocation-dislocation elastic interactions and dislocation line entanglements in the dislocation network.

Captions for Supplementary in-situ **TEM videos**

Supplemental in-situ TEM video 1: In-situ TEM video showing the peeling off of pairs of atomic columns from the (110) surface

Supplemental in-situ TEM video 2: In-situ TEM video showing the birth of a misfit dislocation at the Cu_3Au/Cu(Au) interface via a surface trapping process

Supplemental in-situ TEM video 3: In-situ TEM video showing the nucleation of a misfit dislocation at the Cu_3Au/Cu(Au) interface and its subsequent glide along the Au/Cu(Au) interface

Supplemental in-situ TEM video 4: In-situ TEM video showing the dislocation migration by glide toward the outer (110) surface, which results in the dislocation annihilation at the outer surface

Supplemental in-situ TEM video 5: In-situ TEM video showing the dislocation migration by positive climb into the parent Cu(Au) region

Supplemental in-situ TEM video 6: In-situ TEM video showing the random walk of a dislocation in the parent Cu(Au) region

Supplemental in-situ TEM video 7: In-situ TEM video showing the behavior of a dislocation in the subsurface region during the retraction of a trough-crest reconstructed Cu_3Au(110) ledge on the planar (100) surface

References

1. L. Dong, J. Schnitker, R. W. Smith, D. J. Srolovitz, Stress relaxation and misfit dislocation nucleation in the growth of misfitting films: A molecular dynamics simulation study. *J. Appl. Phys.* **83**, 217-227 (1998).
2. G. Kresse, J. Furthmüller, Software VASP, vienna (1999). *Phys. Rev. B* **54**, 169 (1996).
3. G. Kresse, D. Joubert, From ultrasoft pseudopotentials to the projector augmented-wave method. *Phys. Rev. B.* **59**, 1758 (1999).
4. J. P. Perdew *et al.*, Erratum: Atoms, molecules, solids, and surfaces: Applications of the generalized gradient approximation for exchange and correlation. *Phys. Rev. B.* **48**, 4978 (1993).
5. J. P. Hirth, J. Lothe, Theory of dislocations. (Krieger Publishing Company 1982).
6. P. Williams, Y. Mishin, J. Hamilton, An embedded-atom potential for the Cu–Ag system. *Model. Simul. Mater. Sci. Eng.* **14**, 817 (2006).

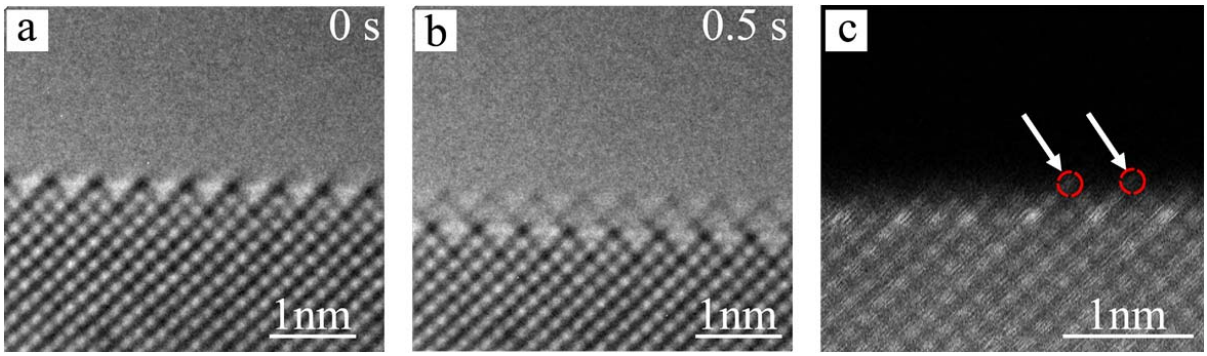

Extended Data Figure 1 | E-TEM and STEM imaging of the e-beam induced edge thinning effect. **a**, HRTEM image showing the trough-crest Cu_3Au surface. **b**, HRTEM image showing the edge thinning effect by deliberately using a strong beam to focus on the edge area. The e-beam induced edge thinning led to the formation of a new (110) ledge that is three atomic layer away from the outmost (110) edge and the Au-segregation along the newly formed (110) ledge resulted in the characteristic trough-crest surface reconstruction. **c**, STEM image of the Au-segregation induced trough-crest surface reconstruction. The white arrows point to the remaining atomic columns on the topmost layer (circled by the dash red rings), while the rest of the atomic columns on the topmost layer were knocked during the e-beam scanning process.

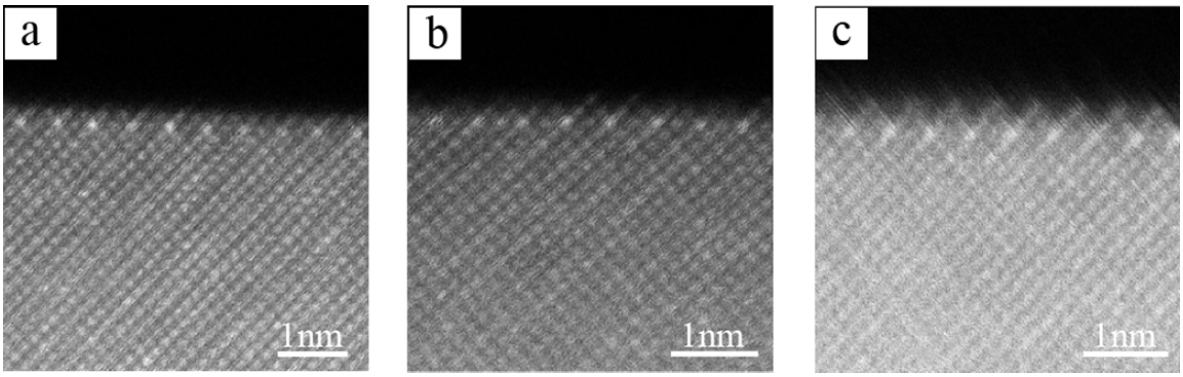

Extended Data Figure 2 | HAADF STEM images of the (110) surface with different inner collection angles. **a-c**, the inner collection angles at 90 mrad, 68 mrad and 54 mrad by using the camera length of 6 cm, 8 cm and 10 cm, respectively. The outermost atomic layer shows a weaker contrast than the inner atomic layers in all the three imaging conditions, indicating that the weakened contrast in the outermost atomic layer is induced by the STEM condensed electron beam effect that resulted in some edge thinning relative to the bulk thin film region.

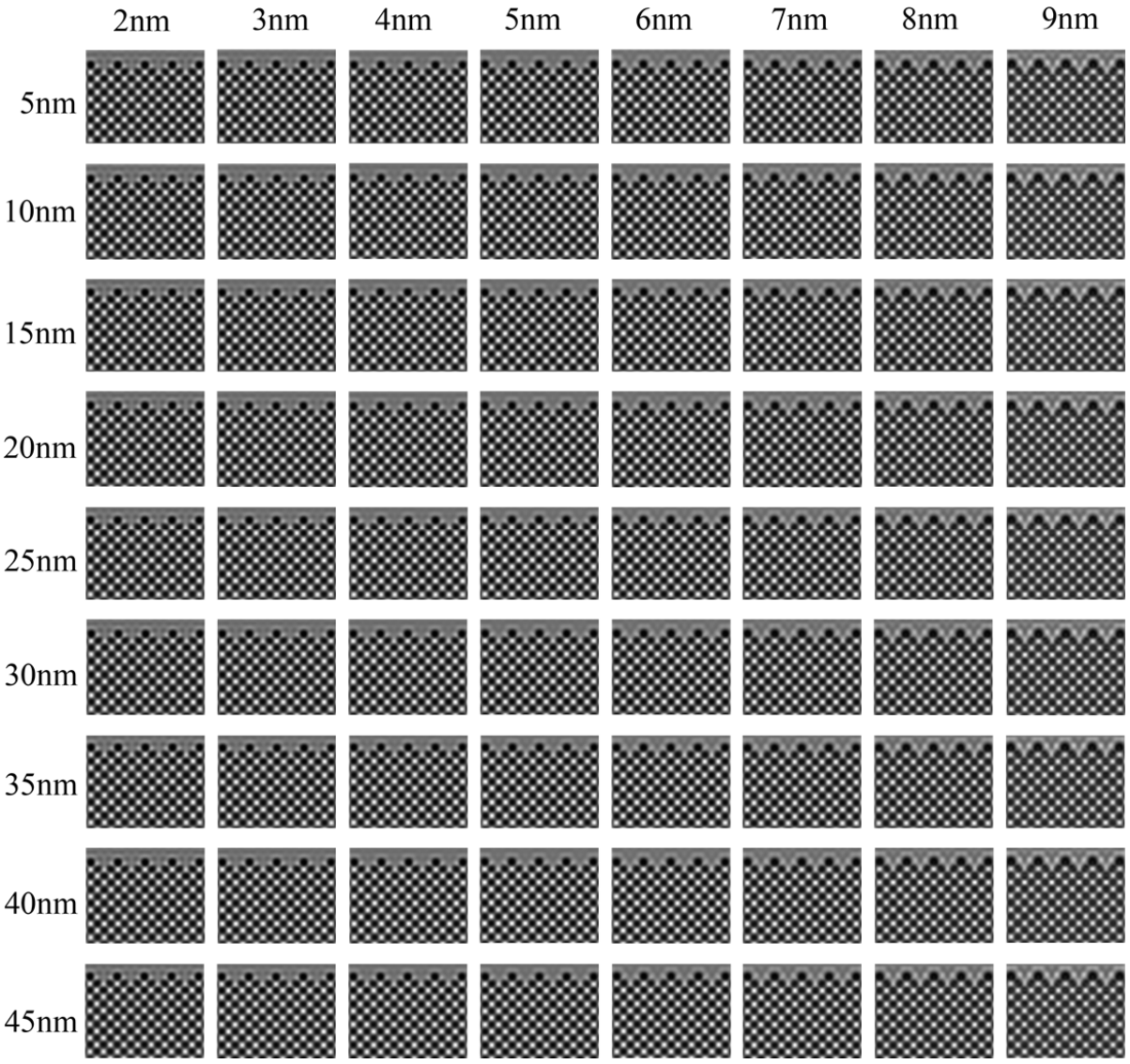

Extended Data Figure 3 | Calculated HRTEM images of the trough-crest reconstructed $Cu_{90}Au_{10}$ surface alloy. The specimen has a bulk thickness of 50 nm (starting from the second outmost layer) with the thickness of the topmost layer increasing from 5 nm to 45 nm (from top to bottom). The defocus value increases from 2 nm to 9 nm (from left to right).

519

520

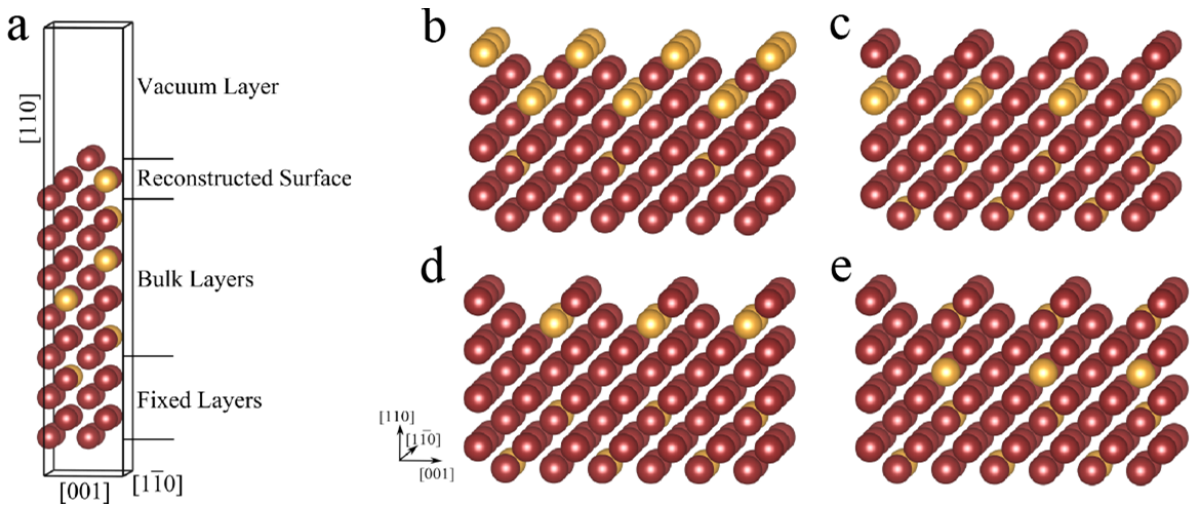

521

522 **Extended Data Figure 4 | a,** Simulation cell used in surface calculations. Cu and Au are presented by the
523 brown and gold spheres respectively. **b-d,** Cu_3Au-type terminations of the reconstructed (110) surfaces of
524 $Cu_{90}Au_{10}$ alloy. **e,** The reconstructed (110) surface of random $Cu_{90}Au_{10}$ alloy.
525

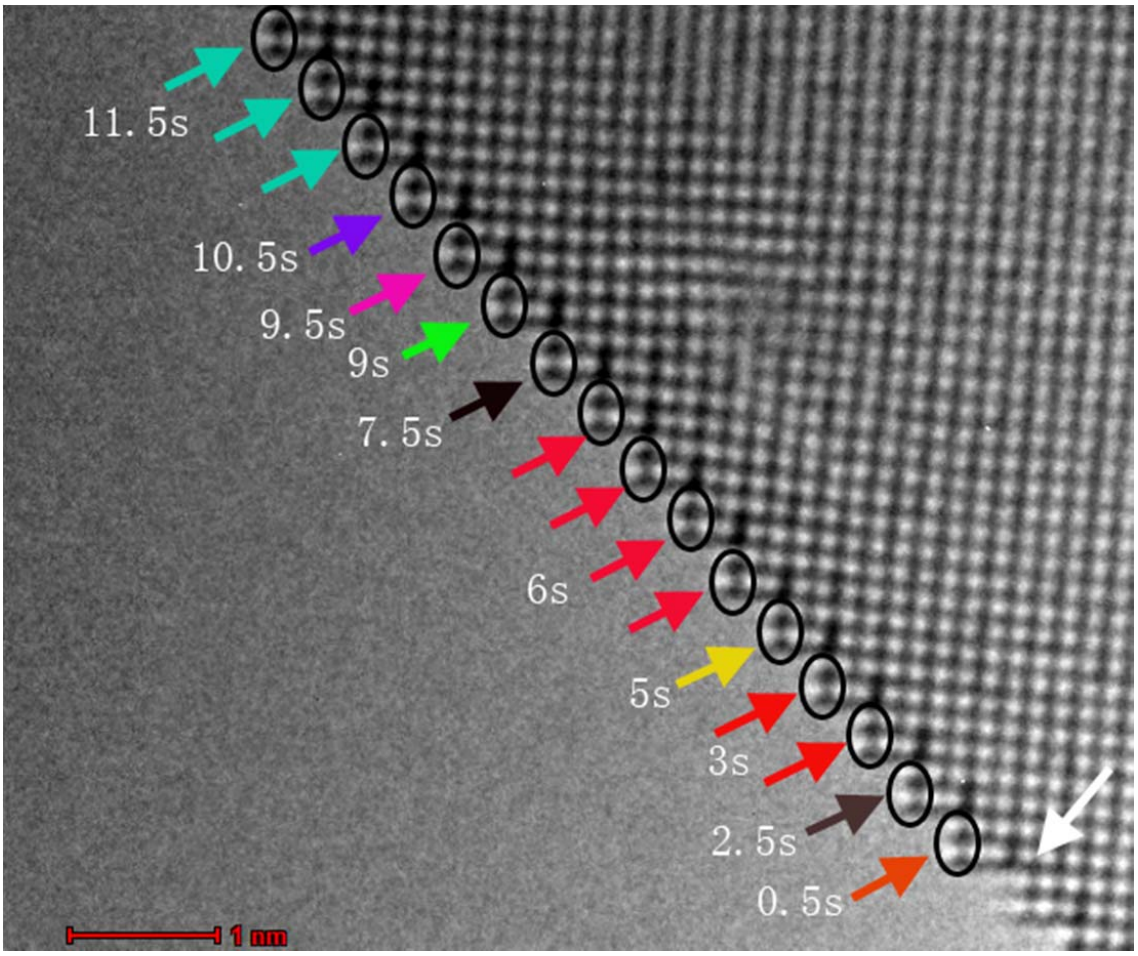

Extended Data Figure 5 | In-situ TEM observations of a {100}-type nano-faceted Au segregated (110) surface at 350 °C and 1×10^{-3} Torr of H_2 gas flow show that surface atoms peel off as pairs of atomic columns from the (110) surface, where the arrows mark the locations and moment of time when the pair of surface atoms peel off from the (110) surface (see Supplemental in-situ TEM video 1).

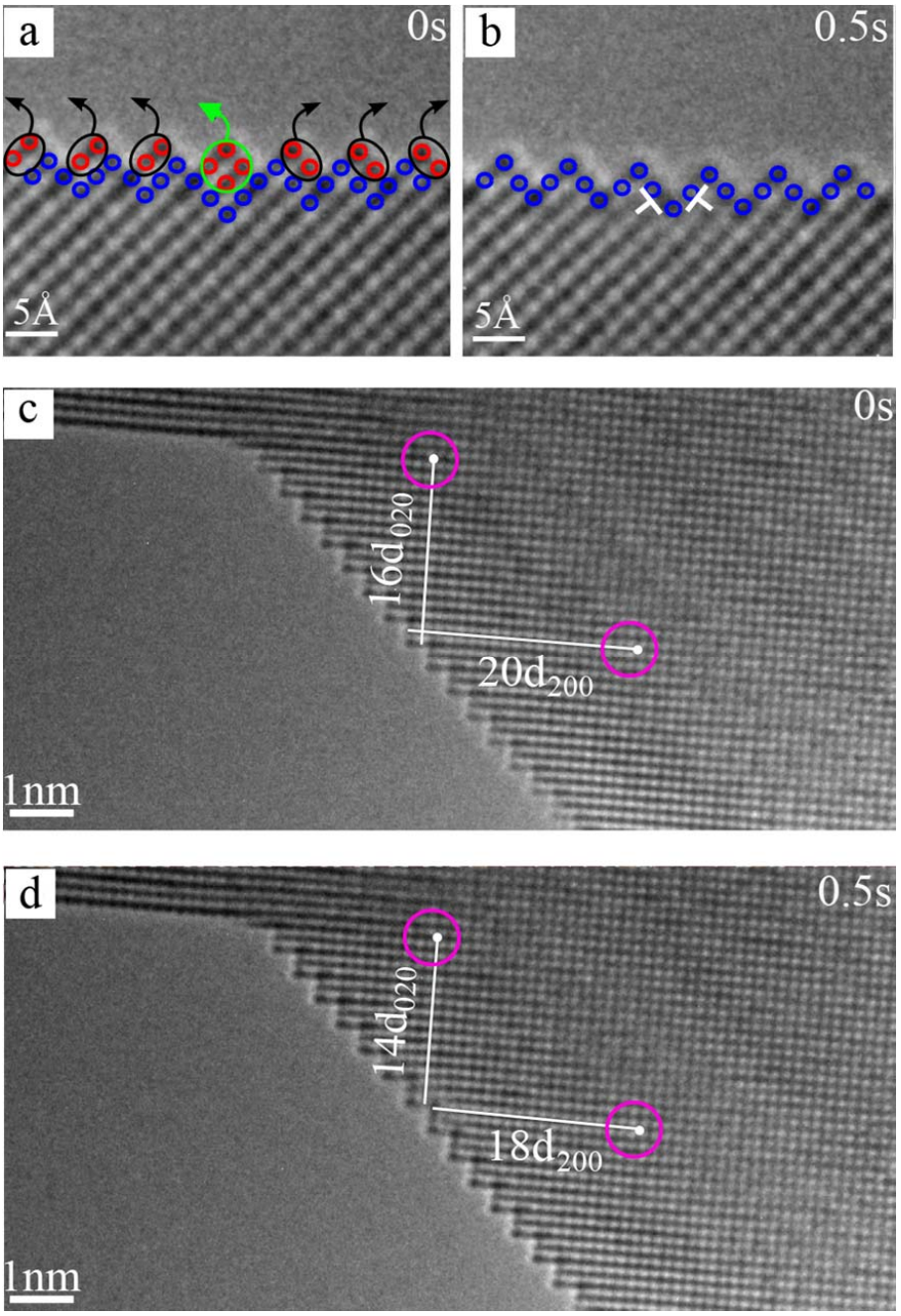

Extended Data Figure 6 | a-b, In-situ HRTEM images capturing the event of nucleating a misfit dislocation in a locally deepened trough formed by the departure of four columns of surface atoms in the region indicated by the large green circle, where the atoms diffusing away are denoted by small red circles and the atoms staying on the surface are denoted by small blue circles (see Supplemental in-situ TEM video 2). **c-d,** Identification of the misfit dislocation nucleation site shown in (**a, b**) by tracking the number of columns of surface atoms departing from the marked region by measuring the change in the distance between the outermost surface and the marked lattice points.

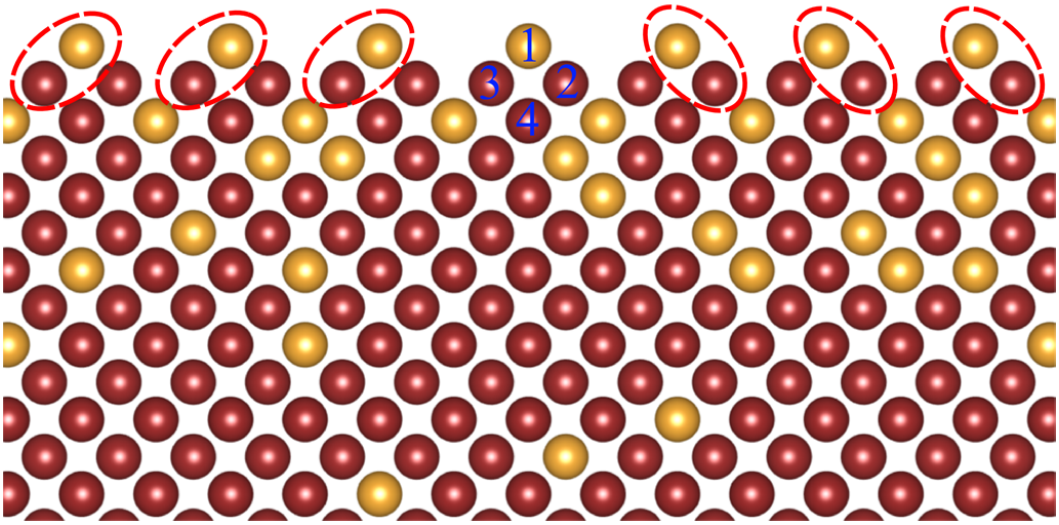

Extended Data Figure 7 | Structure model used for calculating the vacancy formation energy by sequentially removing surface atoms 1-4 from the trough-crest reconstructed surface of the $L1_2$ ordered Cu_3Au segregated layer. The red dashed rings circle out the experimentally observed diatom detachment (see supplementary in-situ TEM videos 1 and 2, and Fig. 2). The energy cost for removing atoms 1-4 is calculated by DFT and listed in Extended data Table 1.

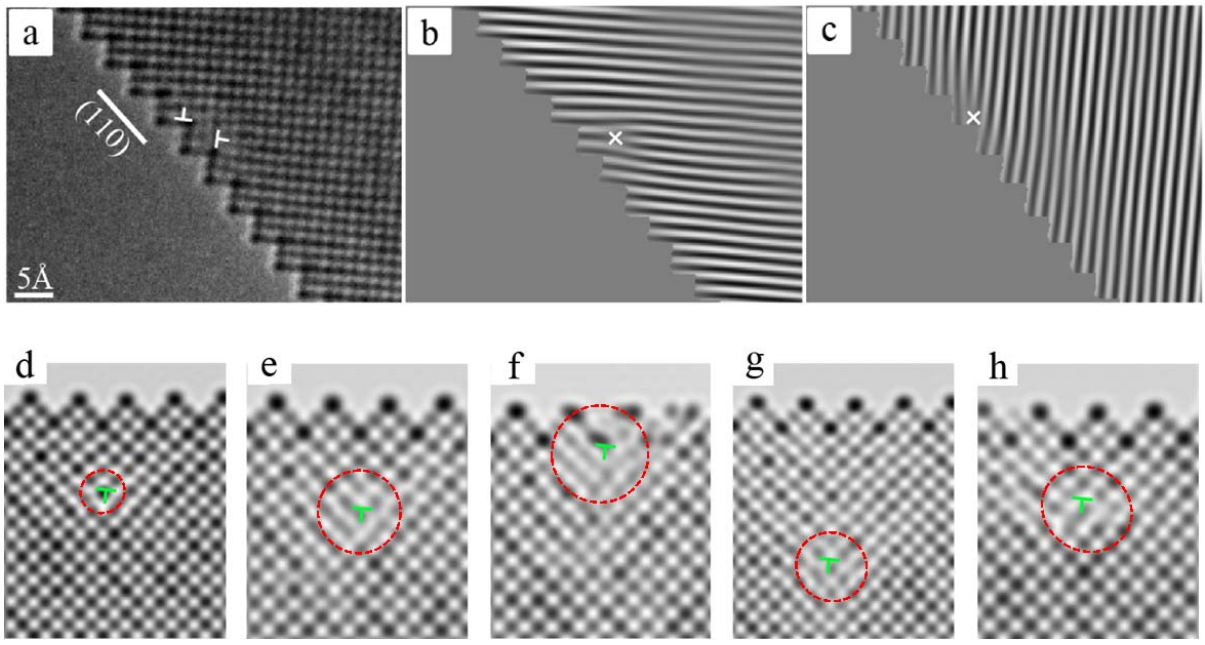

Extended Data Figure 8 | Identification of the location and property of dislocation cores by inverse Fourier-filtered transform (IFFT) and HRTEM simulation. **a,** Raw HRTEM image showing the presence of two dislocation cores residing along the $Cu_3Au/Cu(Au)$ interface. **b,** IFFT operation of the HRTEM using spot mask, white crossover marked the head position of horizontal misalignment, **c,** IFFT operation of HRTEM using spot mask, white crossover marked the head position of vertical misalignment. **d,** the dislocation with the Burgers vector of $b = \frac{1}{2}a[\bar{1}10]$ and dislocation line [001]. **e-g,** the dislocation with the Burgers vector of $b = \frac{1}{2}a[\bar{1}10]$ and dislocation line [111], [112] and [113], respectively. **h,** the dislocation with the Burgers vector of $b = \frac{1}{2}a[\bar{1}12]$ and dislocation line [001].

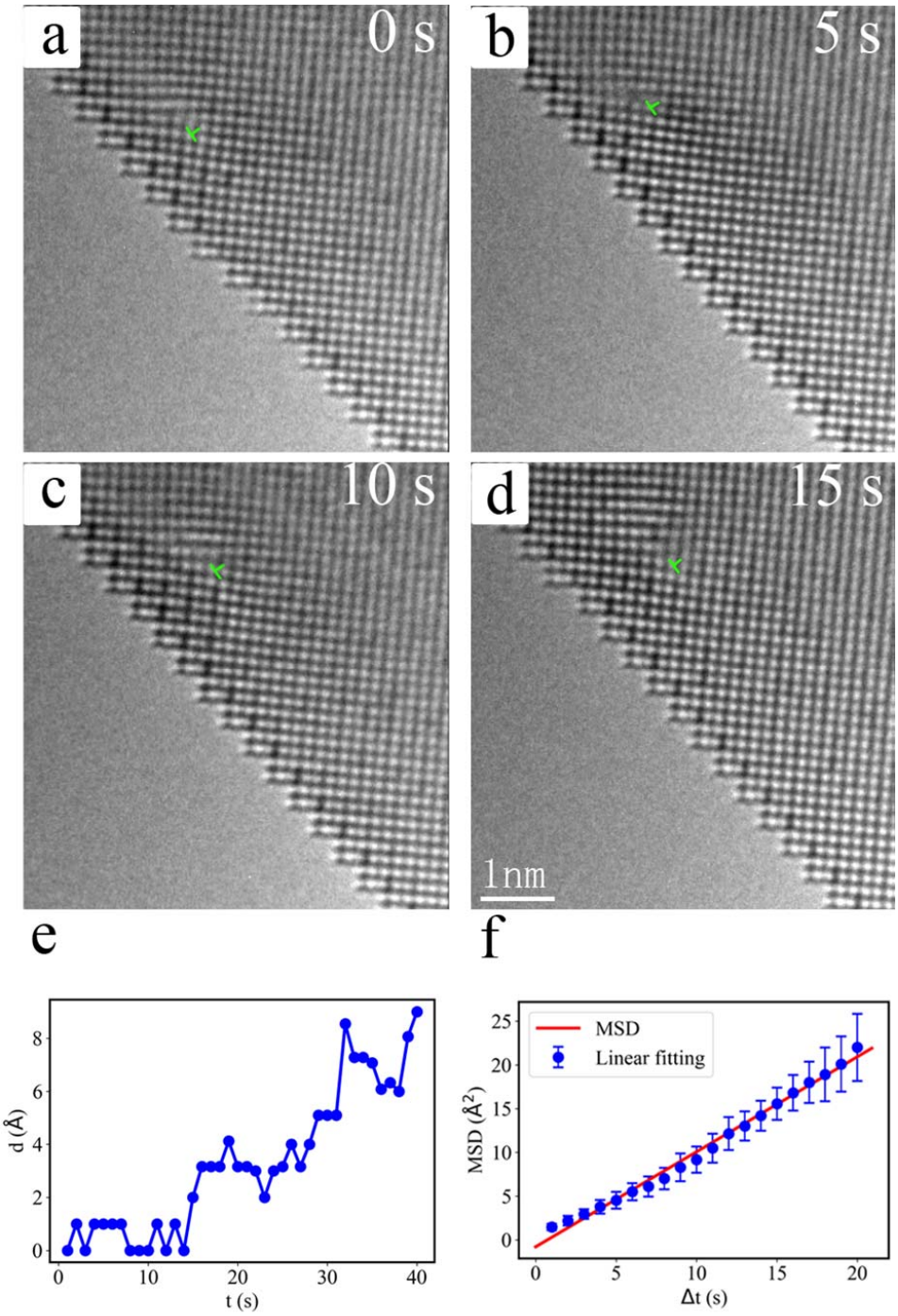

Extended Data Figure 9 | a-d, In-situ HRTEM images showing the migration path of a sessile dislocation (marked by the green "T") in the parent Cu(Au) region at 350 °C and 1×10^{-3} Torr of H_2 gas flow (see Supplemental in-situ TEM video 6). **e,** Distance of the dislocation from its initial position as a function of time. **f,** Mean square distance (MSD) versus time for the dislocation motion, where filled blue squares represent experimental values measured from the in-situ TEM images and solid red line is the linear fit.

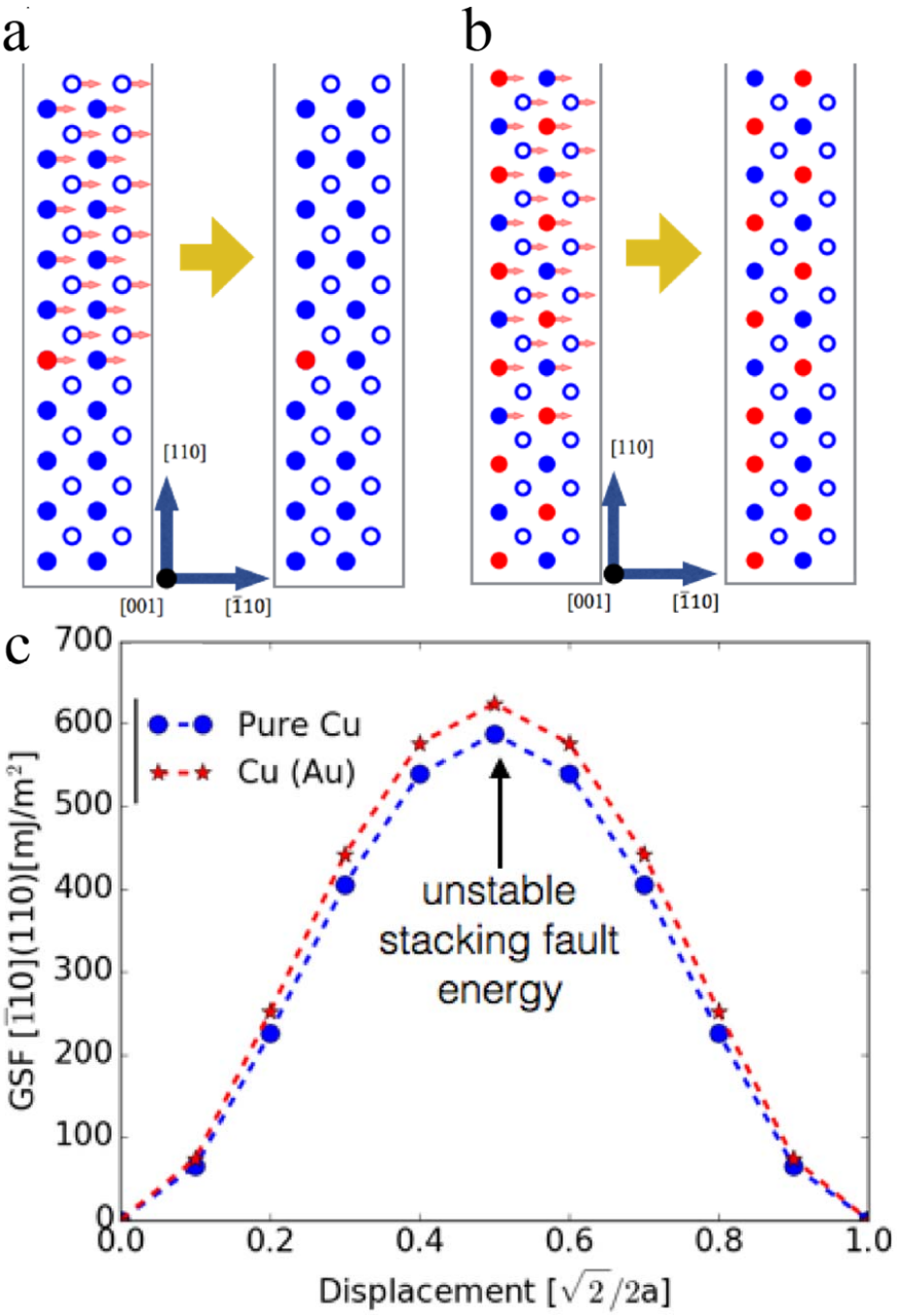

578

579 **Extended Data Figure 10** | **a,** Sketch of the supercells to calculate the GSF in the Cu(Au) system, where
580 the top (110) planes of pure Cu is shifted along the [$\bar{1}$10] direction, with one Au solute atom on the
581 bottom layer nearest to the glide interface. **b,** Sketch of the supercells to calculate APB energies of $L1_2$
582 Cu_3Au, where top (110) planes of $L1_2$ Cu_3Au are shifted by ½ [$\bar{1}$10]. In (**a**) and (**b**), blue color is for Cu
583 and red color is for Au. The filled circles and unfilled circles indicate different atom coordinates along the
584 projection direction perpendicular to the screen. **c,** GSF in pure Cu and Cu(Au) systems calculated from
585 supercells in (**a**).
586

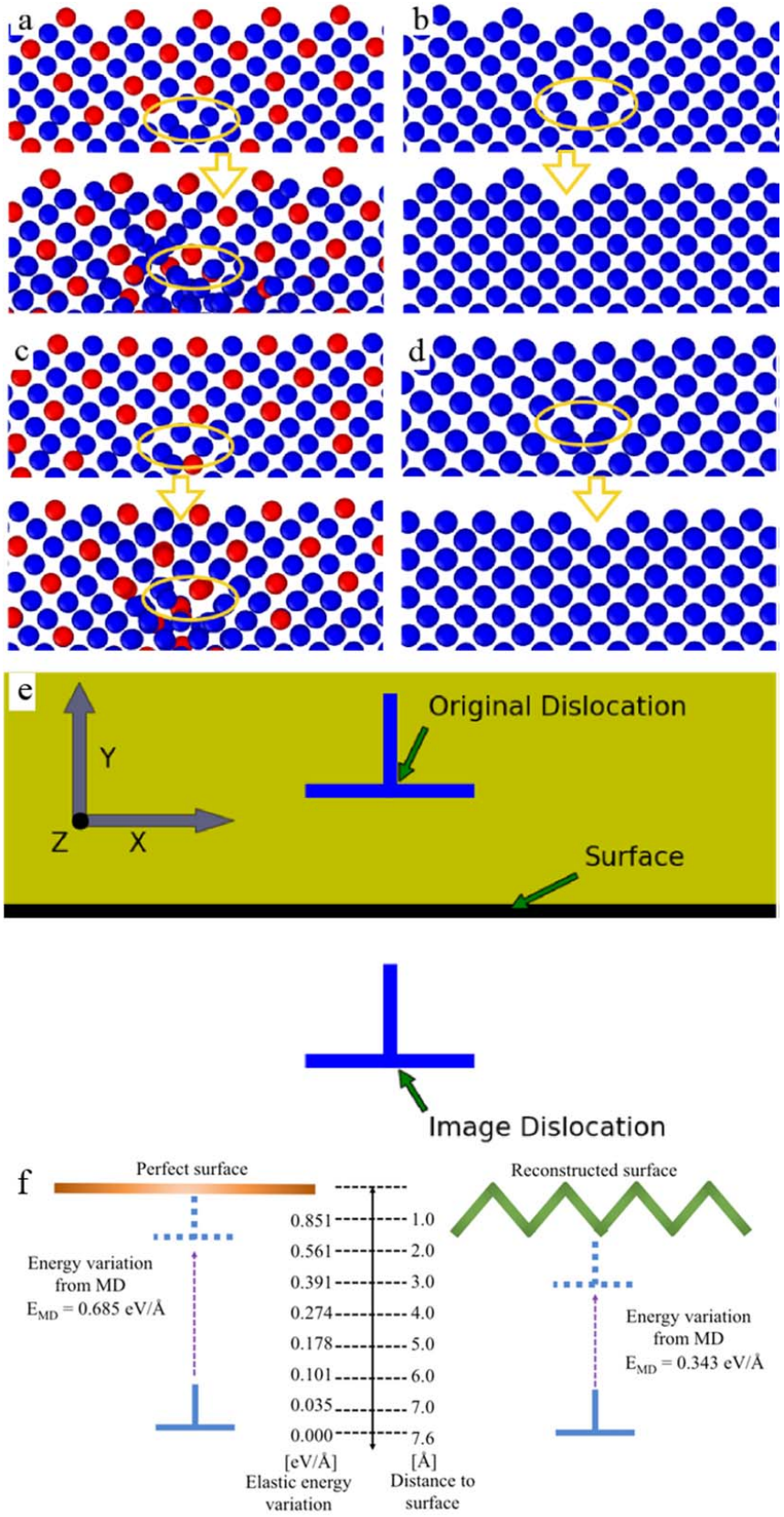

587

Extended Data Figure 11 | ½[$\bar{1}$10](110) dislocation behavior near the surface layers of $L1_2$ Cu_3Au and $L1_2$ Cu_3Ag. a, $\frac{1}{2}a[\bar{1}10](110)$ edge dislocation glides along the Cu_3Au/Cu(Au) interface. **b,** the $\frac{1}{2}a[\bar{1}10](110)$ dislocation in pure Cu annihilates on the free surface by diffusionless transformation. (**a**) and (**b**) are calculated using the CuAu potential. **c,** The $\frac{1}{2}a[\bar{1}10](110)$ edge dislocation glides along the Cu_3Ag/Cu(Ag) interface. **d,** The $\frac{1}{2}a[\bar{1}10](110)$ in pure Cu annihilates on the free surface by diffusionless transformation. (**c**) and (**d**) are calculated using the Cu/Ag EAM potential. **e,** Sketch of the image dislocation of ½[$\bar{1}$10] (111) edge dislocation near the free surface**. f**, Comparisons of energy variations for dislocation annihilation from pure elastic contribution according to Eq. 20 in Extended Data and those from direct MD simulations shown in (b) and (d).

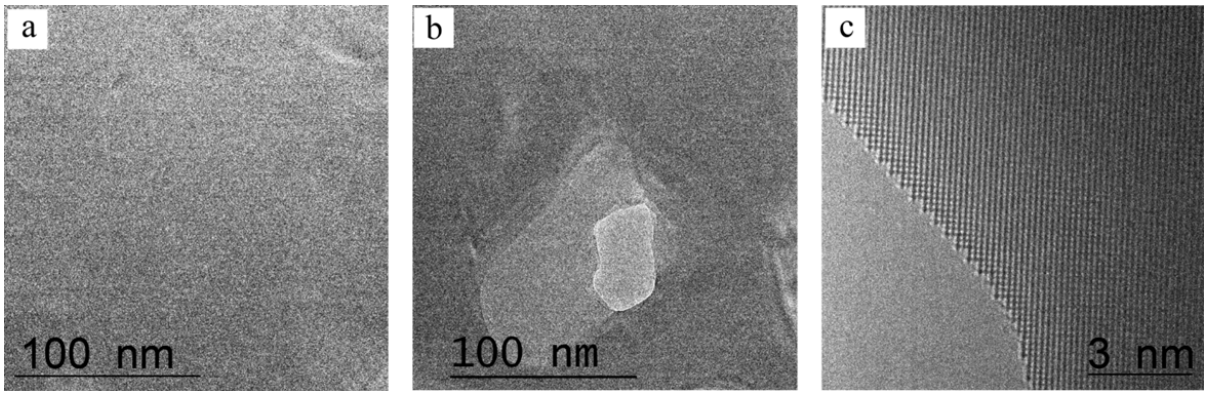

Extended Data Figure 12 | Possible electron beam irradiation effect on the surface structure evolution. **a**, the starting continuous $Cu_{90}Au_{10}$(100) thin film. **b,** Nanopore formation after ~ 20 min of annealing at 350 °C and 0.001 Torr of H_2 gas flow. To avoid any possible electron beam irradiation effect, the e-beam was blanked off during the annealing process. **c**, HRTEM image showing the formation of the characteristic Au-segregation induced trough-crest surface reconstruction of the Cu_3Au surface layer after the e-beam was un-blanked for TEM imaging.

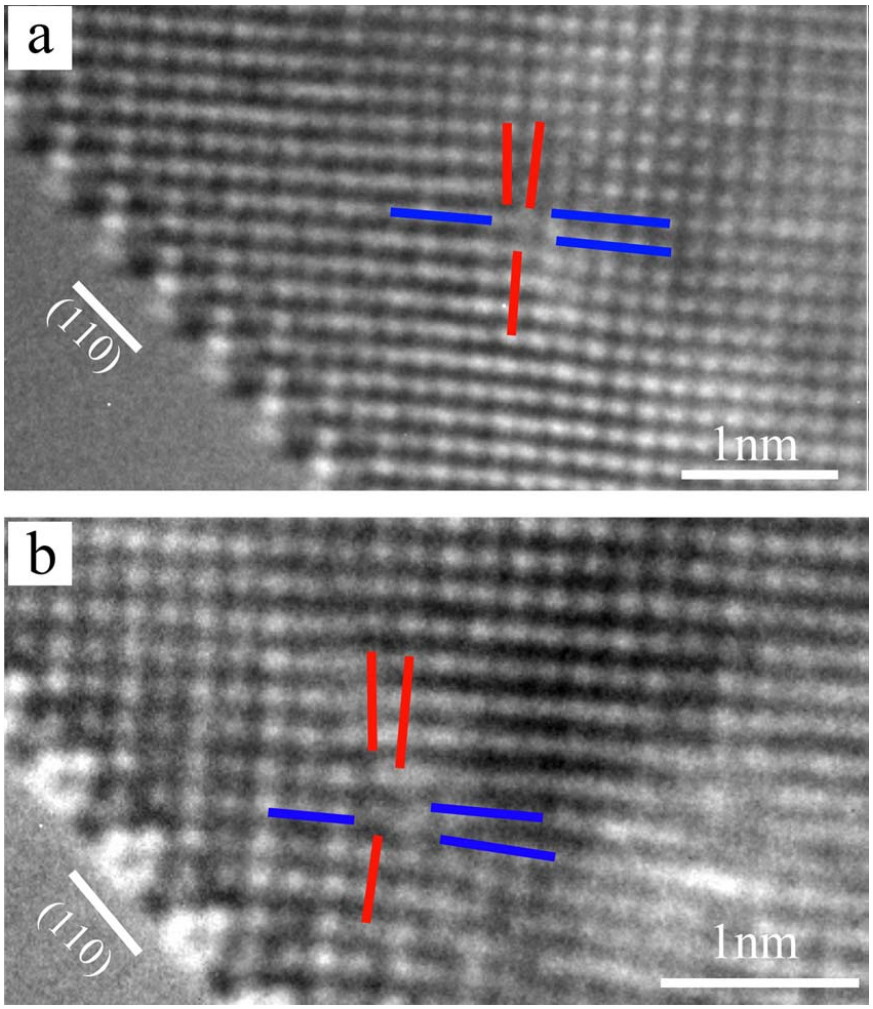

Extended Data Figure 13 | Dislocation motion with blanked electron beam. **a**, $\frac{1}{2}a[\bar{1}10](110)$-type dislocation located in a $Cu_{90}Au_{10}(100)$ film annealed at 350 °C and 1×10^{-3} Torr of H_2 gas flow. **b**, The e-beam was blanked off for a few seconds and then un-blanked for TEM imaging, showing that the dislocation has undergone some migration by moving toward the surface side by a few atomic spacings without the e-beam irradiation.

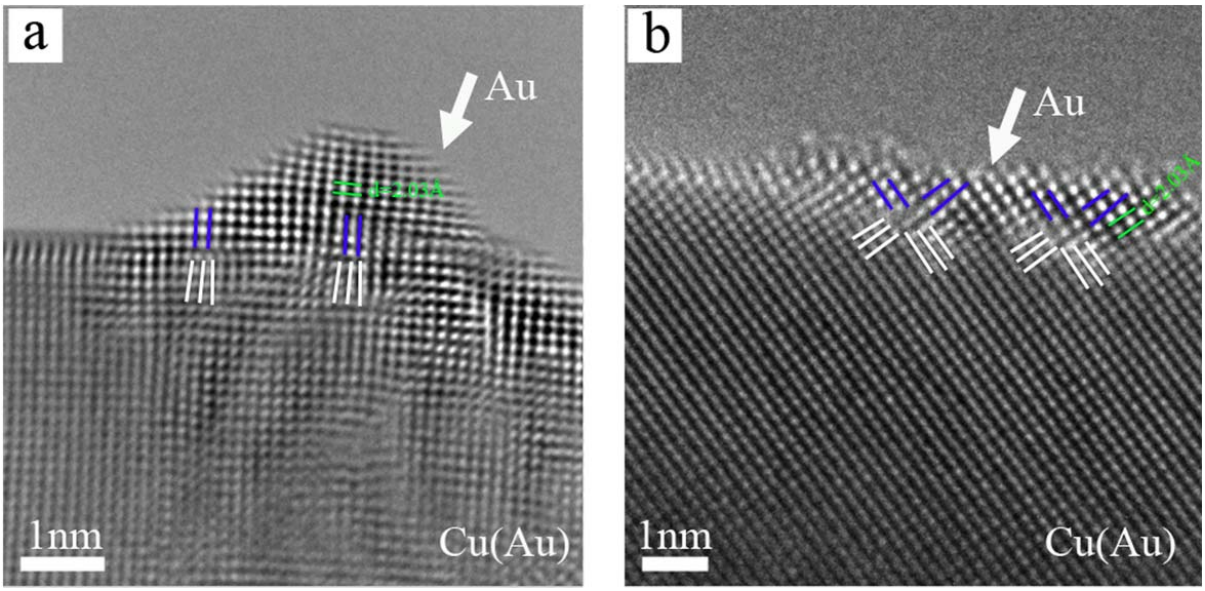

Extended Data Figure 14 | HRTEM images of the Au surface segregation induced Au clusters on the (100) and (110) surfaces at 600 °C and pH_2 = 1×10^{-3} Torr. **a,** misfit dislocation array formed along the [100] direction of the Au/Cu(Au) interface. **b,** misfit dislocation array along the [110] direction of the Au/Cu(Au) interface. The lattice mismatch at the Au/Cu(Au) interface is marked by the blue and white line.